FIGURE 5 Clinical predictions based on the assessment of epithelial and mesenchymal senescent metastatic cancer cell (SMCC) signatures in colorectal liver metastasis (CRLM) and TCGA-CRC cohorts. (a) 5-multilabel immunohistochemistry for $p21^{Cip1}$, $p16^{Ink4a}$, $p15^{Ink4b}$, γH2A.X, and ki67 performed over 68 CRLM patients, randomized in chemo and not chemo treated, bar 200 μm. (b) Overall quantification in SMCC subgroups of the CRLM cohort. (c) Quantification of $p21^{Cip1}$ and $p16^{Ink4a}$, $p15^{Ink4b}$ markers. Wilcox.test, $^{****}p < 0.0001$ (d) ki67 and (e) γH2A.X quantification over the SMCCs groups. Wilcox.test, $^{*}p < 0.05$; $^{**}p < 0.01$; $^{***}p < 0.001$. (f) Overall survival (OS) Kaplan–Meier curve of CRLM patients: peto-peto, $^{*}p < 0.05$. (g) Disease-free survival (DFS) Meier curve relative to the same CRLM cohort. OS Kaplan–Meier curve (h) and DFS-Meier curve (i) for the eSMCC signature. (j) OS and (k) DFS Kaplan–Meier curves for mSMCCs signature over TCGA-CRC cohort ($n = 362$). Significance of chemotherapy treatment for $eSMCC^{high\text{-}low}$ (l) and $mSMCC^{high\text{-}low}$ (m) signatures related to fluorouracil and oxaliplatin-specific drugs.

In contrast, the eSMCC ecosystem, deficient in TGFβ1, had active immune flow in which T and NK cells as well as their cytotoxic product Granzyme B accumulated massively (Figure 6d,h and Figure S6k). To validate our ST data, we performed a co-staining between M2 and CD4/CD8 markers on meta1 (Figure 6i). As predicted, CD163-positive macrophages (red) accumulated around the mSMCC crypts, that were enriched in CD4-positive cells (green), whereby eSMCCs showed higher CD8 infiltration and less CD163 accumulation in the ECM. Finally, we extended this analysis in our CRLM cohort (Figure 6j and Figure S4b, $n = 5$ for group). As expected, the four groups acted distinctly for GZMB, PD-1 and CD163 markers in terms of expression and distribution (Figure 6k–m). In the eSMCCs group, GZMB colonized the entire metastasis, while for PD-1, most of the patients showed lower intrametastatic expression compared to mSMCCs. Only one eSMCC biopsy did not reflect this trend. M2 cells were scarce in both intra- and perimetastatic areas. In the mSMCCs group, GZMB and CD163 accumulated significantly in the perimetastatic zone, while PD1 was abundantly found in and out of the metastasis, suggesting the establishment of an immunosuppressive environment. Notably, in negative patients, we observed a conserved accumulation of immune cells in the perimetastatic area compared to the intrametastatic zone for all the immunogenic markers. The fact that the Neg group mimicked GZMB and CD163 mSMCC distribution, but not PD-1, could partially explain the discrepancy in the impact on relapse showed in Figure 5g. Finally, Mix's patients resembled eSMCCs group trend for cytotoxic and immunosuppressive markers, but at lower levels, and for M2 in the intrametastatic area, while recruiting more M2 in the perimetastatic zone (Figure 6k–m). The three patients with spatially isolated SMCCs signatures recapitulated the corresponding immunogenic findings (Figure S4b).

3 | DISCUSSION

This study exploits spatial transcriptomics to decipher the biological significance of senescent cancer cells throughout CRC evolution, finding that SMCCs are leading players in metastasis and tumor outgrowth. The novelty of our work resides in the discovery that the clinical outcomes of CRC and CRLM depend on these non-proliferating cancer cells. Neo-adjuvant chemotherapy, the gold-standard therapy for CRLM, consists of the administration of anti-proliferative drugs to reduce tumor size and allow easier metastasis resection. Our findings suggest that this first hit could compromise patient fitness, encouraging the establishment of an mSMCC phenotype, which would determine a fatal outcome. The choice of specific chemotherapeutic agents has to be carefully weighted from clinicians before any clinical intervention, due to their impact on mSMMCs incidence.

It would be important to understand whether eSMCC and mSMCC populations evolve reciprocally, as the EMT trajectory suggests. The partial overlap between SMCCs and Doxo-induced signatures might suggest that those two processes can be concomitantly active. However, it is difficult to establish whether the distinct mechanisms of senescence induction, cell autonomous versus paracrine, are biologically coordinated and what could determine the complete evolution from a Mix to a "pure" signature. The absence of a clinical predictive role for iSMCCs or not-SMCCs would further support the complexity of senescence behavior in cancer. Indeed, cells with EMT hybrid signatures have shown more effectiveness in circulation, colonization and development of metastasis (Pastushenko et al., 2018). However, we are aware that our evaluation is limited to CRC samples.

Research focuses on genetically aggressive variants that confer a transcriptional survival advantage (Birkbak & McGranahan, 2020; Giessler et al., 2017; Jones et al., 2008). We found no differences in the transcriptional signature of senescent cancer cell subtypes in primary versus secondary organs, meaning that some cancer cells are "born to be bad." The clinical outcome seems to be determined by the percentage of SMCC subtype within cancer. However, which factors determine the multicellularity of metastasis and the kinetics of progression need investigation. Whether the predictive power of SMCC signatures depends on origin (epithelial or mesenchymal) or is more strictly related to senescence is another open question. Our findings suggest that SASP is linked to stressor type rather than cell origin. Indeed, eSMCC SASP overlaps with RAS-induced senescence in fibroblasts rather than with IRR epithelial cells. Evidence for a connection between senescence and EMT comes from the observation that transcriptional signaling driving senescence is also involved in EMT (Smit & Peeper, 2010). Therefore, sharing a commitment to cancer progression is indisputably a functional overlap (Muñoz-Espín & Serrano, 2014).

Therapeutically, the presence of eSMCCs is a desirable final stage, recalling the historical role of senescence as being tumor-protective (Bennecke et al., 2010; Sieben et al., 2018). Regarding the detrimental outcome of mSMCCs, there are at least three hypotheses: (i) mSMCCs are linked to an intermediate stage of EMT, and, therefore, to a reversible process, under which cells undergo transcriptional-EMT chromatin reorganization. Effectively, in several human pathologies and experimental models, tumor cells are

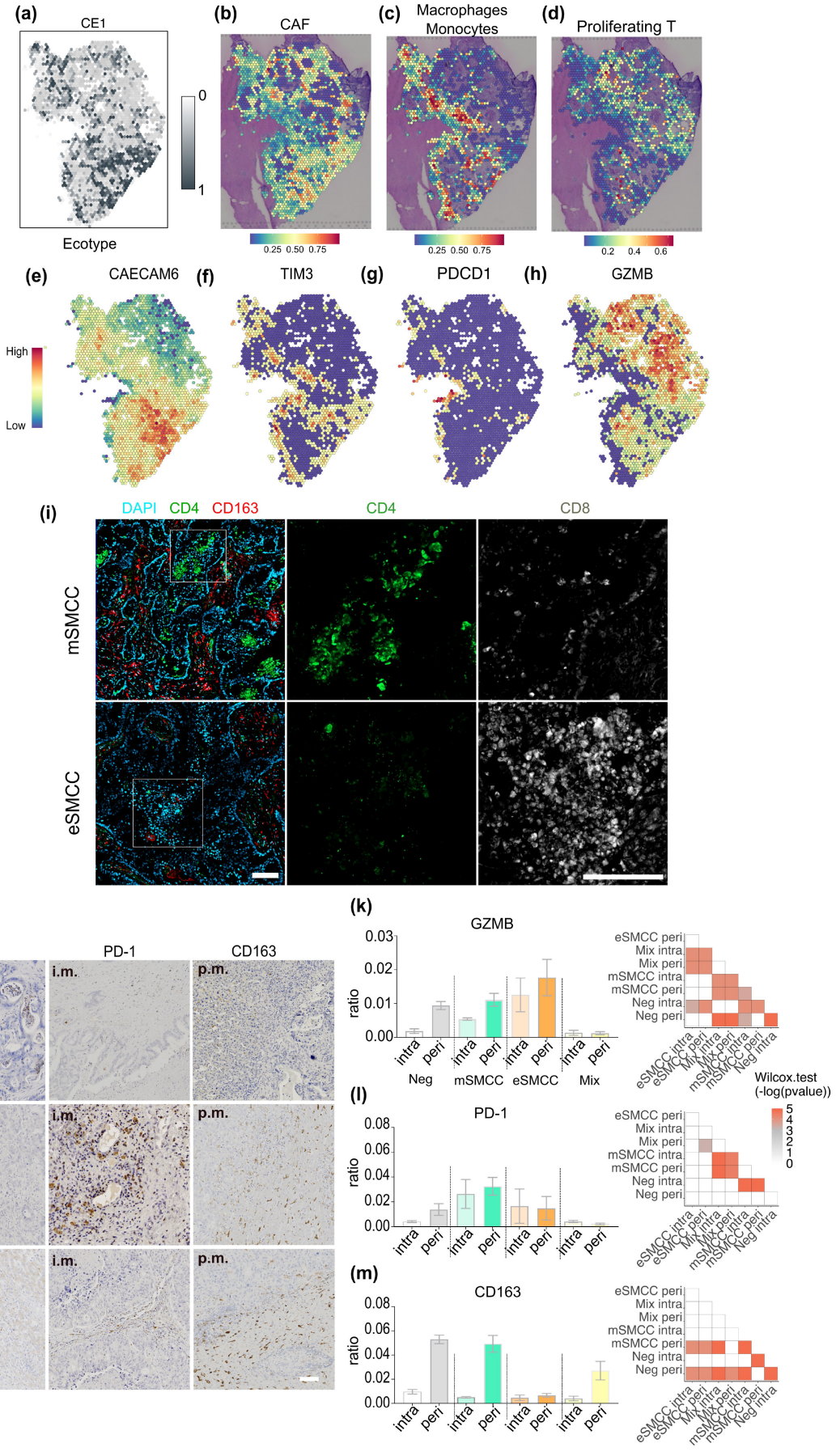

FIGURE 6 Immuno-modulation properties of epithelial versus mesenchymal senescent metastatic cancer cells (SMCCs) in colorectal liver metastasis (CRLM). (a) CE1 ecosystem produced by ecotype analysis. (b) Integrated analysis of spatial data and single-cell extracellular matrix (ECM) signatures from an independent CRLM study, showing CAF localization over meta1. Integrated analysis of spatial data and immune single-cell signatures from an independent CRLM study, showing (c) macrophages and (d) proliferating T-cell localization over meta1 specimen. Immunosuppressive (e–g) and (h) cytotoxicity markers activity maps localized in mSMCCs and eSMCCs ecosystems, respectively. (i) Z-stack projection of CD4, CD163, and DAPI co-staining on meta1 cryosection (left). CD4 and CD8 immunofluorescence corresponding magnifications (right). CD8 antigen immunostaining was performed on meta1 serial cryosection, bars 100 μm. (j) Immunohistochemistry for GZMB, PD-1, and CD163 over our CRLM cohort ($n = 5$ for each group), showing that meta1 findings are reproducible. GZMB, shown in the intrametastatic area (i.m.), accumulates in eSMCCs comparing other groups. PD-1 is shown in the i.m., while CD163 is shown in the perimetastatic area (p.m.). Digital quantification of GZMB (k), PD-1 (l), and CD163 (m) markers randomized in intrametastatic and perimetastatic areas in epithelial and mesenchymal SMCCs, Negative and Mix patients. On the right, heatmap of Wilcoxon test applied to the data reported on the left (k–m). The values <−log(0.05) were considered not significant and reported in white.

released from senescence with high aggressive growth phenotype (Milanovic et al., 2018; Roberson et al., 2005; Saleh et al., 2020). Additionally, cellular senescence has been described as the steady state of somatic cell reprogramming, that if overcome would allow an efficient transition to a stem-cell phenotype (Li et al., 2021). Those findings underlie the unexpected plasticity of senescent status, which represents a bottleneck for multiple cell-type transitions. (ii) mSMCCs could become "revertant" cells, that is, cancer cells with low proliferating ability but highly increased migration and invasion (Yang et al., 2017); and (iii) mSMCCs could be irreversibly arrested in G1, but could forage the non-senescent cancer cells to survive. In any case, senolytics tailored to the mSMCC molecular signature represent a novel area of investigation for the development of effective CRLM therapies.

One of the limits of our ST approach is the lack of single-cell resolution, which restricts the findings on small cells and in the case of overlapping signatures masks the weakest or the less representative ones. By integrating our spatial transcriptome with single-cell RNAseq CRLM-derived immune subpopulation, we observed different immune landscapes around SMCCs areas, confirmed by immunohistochemistry. It is tempting to speculate that, as for primary CRC, CSF1 secreted by mSMCCs could drive M2 macrophage polarization, resulting in $CD8^+$ T cell inhibition (Choi et al., 2021). Further studies are required to dissect the contribution of SMCCs to immune response. Recently, immunogenic properties of senescent cells have been validated in experimental murine models and human cancer cell lines (Chen et al., 2022; Marin et al., 2023). Whether those properties are relevant to CRLM pathology needs to be properly investigated. Additionally, understanding how targeting senescent cancer cells impacts tumoral immune microenvironment or how the immune system can be harmed to drive the clearance of bad SMCCs will be crucial to enroll senotherapies for clinical trials (Amor et al., 2020; Waldman et al., 2020).

We have deciphered here the significance of the spatial organization and transcriptional program of senescent cancer cells in colorectal liver metastasis. We have elucidated the microenvironmental landscape, including secretory properties and TME–cell interactions. We have demonstrated that SMCCs play an important role in shaping the physical outgrowth of metastasis. The coexistence of two SMCC populations with opposing effects can explain heterogeneity in relapse and drug resistance. Individually, SMCC signatures have a consistent prognostic role in all the steps of CRC evolution, highlighting their significance for the development of new therapeutic approaches in colorectal liver metastasis.

4 | METHODS

4.1 | Human samples

From the existing database at the IRCCS Humanitas Research Hospital, we have retrieved 68 patients according to the following inclusion criteria: histologically proven diagnosis of CRLM; availability of the full data for analyses including follow-up. Diabetics, obese, HCV-positive, HBV-positive, and alcohol abusers were excluded. All patients were further randomized into Group A (patients treated only with hepatectomy) and Group B (patients treated with neo-adjuvant chemotherapy followed by hepatectomy). The biological specimens consist of CLM tissue and normal non-tumoral adjacent liver parenchyma. Additional 32 subjects were also enrolled with histologically proven diagnoses of CLM. The CLM specimens, consisting of CLM and corresponding non-tumoral hepatic parenchyma, were analyzed in part for β-gal positivity, and in part for spatial transcriptomic technology. β-gal stained sections were subjected to pathology review to confirm that the positivity for cellular senescence marker was histologically consistent with the tumoral part and does not belong to other histological compartments.

All patients were enrolled into the clinical protocol entitled "Studio dell'interazione tra la senescenza cellulare e sistema immunitario nelle metastasi epatiche umane da tumore primario al colon: alla scoperta di un nuovo possibile marker prognostico," which was approved and registered by the local institutional ethical committee (Humanitas 564/21). Each patient signed a written informed consent for general research purposes. Demographics and clinical characteristics from the retrospective cohort and the freshly removed specimens with β-gal scoring are in Table S1.

4.2 | Methods details

4.2.1 | Collection and preparation of CRLM tissue for spatial transcriptomic

The CRLM specimens have to be processed within 30 min from the surgical removal and for β-gal enzymatic assay. Those are the best practices for preserving RNA integrity and β-gal enzymatic activity, which would become undetectable after only one night at −80°C. CRLM specimens were embedded in Optimal Cutting Temperature (OCT) compound and snap-frozen in a bath of Isopentane (2-Methylbutane) and liquid nitrogen. Four serial sections for each specimen were immediately cryosectioned at 10 μm thickness. Three sections were processed for RNA Integrity Number (RIN), one for β-gal assay. Cardinal points were signed on the OCT blocks, to re-place the tissue block on the cryostat stage with the initial orientation, for the sectioning of desired areas identified after β-gal staining.

4.2.2 | RNA quality assessment

The RNA was isolated using Qiagen RNeasy Mini Kit (Cat#74104), following manufacturer's recommendations. RNA quality control was performed with the Agilent 4200 Tape Station system using the High Sensitivity RNA ScreenTape (5067-5579) analysis kit (Agilent); only RNAs having a RIN ≥7 were used for Spatial transcriptomic technology.

4.2.3 | Tissue optimization protocol

This step was necessary for the optimization of permeabilization procedure, which is tissue-dependent. We employed ad hoc Visium Spatial Tissue Optimization Slide which contains canonical Capture Area printed with capture sequences for mRNA capture but lacks spatial barcode array. The procedure involved testing times of 60, 45, 30, 20, 10, and 5 min on serial cryosection of a CRLM sample. The release step of the surface probes was not performed, and the reverse transcription mixture contained the same reagents except for 0.5 mM of each dATP/dGTP/dTTP, 12.5 μM dCTP, and 25 μM Cy3-dCTP. Glass slides were scanned in AxioScan microscope. Dim and low fluorescence signals indicative of suboptimal permeabilization were excluded; we established that the best condition for CRLM was 15 min of enzymatic digestion.

4.3 | Spatial transcriptomic procedure

We select 4 CRLM samples based on RIN >7. Two of them were also pre-screened for β-gal assay resulting in positive. We mounted the selected OCT tissue blocks on the specimen stage aligned as previously based on cardinal signs and cut serial cryosections which have been placed onto Tissue Preparation Guide (CG000240). For the following steps, we acted by Visium Spatial Gene Expression protocol (CG000239) with minor modifications.

4.3.1 | Staining and imaging

Visium Spatial Gene Expression slide, containing the four CRLM sections, was incubated following the Methanol Fixation + H&E Staining guide (CG000160). Finally, the slide was dried at 37°C for 5 min and mounted with Mounting Medium (22.5 μL RNase inhibitor, 7.5 μL Nuclease-free water and 170 μL Glycerol). The slide was imaged with AxioScan, in brightfield with 20× magnification. After acquisition, the Spatial Gene Expression slides were immersed in a 3× SSC solution in ultrapure water for 20 min, to remove the coverslip.

4.3.2 | Permeabilization, reverse transcription, denaturation, and cDNA generation

Permeabilization enzyme was equilibrated at 37°C for 15 min before proceeding. The slide was assembled into the Visium slide cassette to perform the enzymatic reaction on a thermocycler adaptor. Seventy μL of Permeabilization enzyme was uniformly added to each well, and the Visium slide cassette was incubated on a thermal cycler at 37°C for 15 min. Following Permeabilization step, we performed Reverse Transcription, Second Strand Synthesis and Denaturation. cDNA generated was transferred in a pcr tube from the slide. One spatially barcoded full-length cDNA was amplified for 12 cycles and the other three cDNA for 14 cycles determined on the C_q value by qPCR amplification plots following the manufacturer's protocol (CG000239). After, the cleanup by SPRIselect beads, we evaluated the cDNA concentration by Qubit dsDNA HS Assay Kit (Q32854); a quality profile was performed with the Agilent 4200 Tape Station system using the High Sensitivity D5000 ScreenTape (5067-5592) analysis kit (Agilent).

4.3.3 | Library construction and sequencing

Twenty-five nanogram of the amplified cDNA was then used for each sample to construct Illumina sequencing libraries following the manufacturer's protocol (CG000239) using 17 cycles and Dual Index Plate TT set A for their generation. Final libraries were checked by Qubit dsDNA HS Assay Kit (Q32854) and the Agilent 4200 Tape Station system using the High Sensitivity D5000 ScreenTape (5067-5592) analysis kit (Agilent). Sequencing was performed on the NextSeq550 Illumina sequencing platform following the run parameters such as Reads1 = 28; i7Index = 10; i5Index = 10; Reads2 = 90 and calculating sequencing depth requires estimating that the approximate capture Area covered by tissue is about 85%.

4.3.4 | Immunohistochemistry

Immunohistochemical analysis of CRLM tissues was performed on FFPE 3-μm-thick serial sections. The FFPE sections were deparaffinized, pre-treated with Target retrieval solution, ph9 (1×) at 98°C (20 min) and then incubated o/n at 4°C (or 1 h a RT for γH2A.X antibody) with primary antibody anti-human ki67 (DAKO, #F7268, 1:200), anti-human CK20 (DAKO, # M7019, 1:200), anti-human $p21^{Cip1}$ (DAKO, #M7202 1:200), anti-human γH2A.X (Cell signaling, #9718, 1:500), anti-human NOX4 (Abcam, # 133303, 1:200) and anti-human $p15^{Ink4b}$ (Orbit, orb30654, 1:50). The antibodies were diluted in Universal Antibody Dilution Buffer. For anti-human $p16^{Ink4a}$, serial sections were pre-treated with DIVA retrieval solution at 98°C (20 min) and then incubated for 1 h a RT with primary antibody (ready to use provided). For Granenzyme B (R&D, AF1865, 1:200) and CD163 (Leica Biosystems, PA0090, 1:200) antibodies, tissue sections were pre-treated with Citrate solution at 98°C (20 min) while for PD1 antibody (ab52587, 1:100) with DIVA Decloaker solution (Biocare Medical, SKU DV2004) and then incubated o/n at 4°C with primary antibody. Endogenous peroxidase was blocked for 20 min in Real Peroxidase blocking solution.

Envision + System HRP Labeled Polymer anti-Mouse, anti-Rabbit, or anti-Goat HRP-Polymer kits was used as a secondary antibody, depending on the species of the primary antibody. After washing, slides were developed with DAB (3,30-diaminobenzidine) (Betazoid DAB Chromogen Kit; Biocare Medical #BDB2004) and counterstained with Hematoxylin. Tissues were dehydrated with ethanol, mounted with Eukitt, and analyzed with an Olympus BX61 virtual slide scanning system or Axio Scan. For $p21^{Cip1}$ (Origene, TA808128, 1:150) staining on Doxo-treated cells, we applied the same conditions described above for tissue, avoiding the antigen retrieval treatment.

4.3.5 | Images analysis

To obtain the immune reactive area for each marker, tissue slides were digitized after staining procedure using a computer-aided slide scanner (Axio Scan). An expert pathologist selected the same areas which overlapped with the previous staining for $p16^{Ink4a}$, $p21^{Cip1}$, $p15^{Ink4b}$, and γH2AX. Since most CRLM patients receive neo-adjuvant systemic chemotherapy leading to tumor necrosis to variable extents, we avoid necrotic areas often found in the tumor core region. The pathologist defined the peritumoral region based on a manual definition of the tumor and extracellular matrix surrounding the crypts. An image analysis software (QuPAth) was used to automatically determine the percentage of immune reactive area of the digitized images. The mean value, obtained from the three different microscopic areas, was calculated for each patient and used for subsequent analyses. With these criteria, we establish the immunogenicity of our patients accordingly to the previous classification in eSMCCs, mSMCCs, Mix and negative. Five patients representative of each category were analyzed.

4.3.6 | Immunofluorescence

The protocol for serial cryosection and HCT-116 cells differs only for the mix of primary antibodies applied. The material was fixed at 4°C for 5 min in 4% of paraformaldehyde. Then, after three washes in PBS1× (5 min each), it was permeabilized in ice-cold acetone for 5 min. After three washes in PBS1× (5 min each), the section was incubated for 30 min with blocking solution at room temperature (2.5% Bovine serum albumin in PBS1×). The cryosection was incubated for 1 h with anti-human RPL11 (Thermo Fisher, Cat# PA5101381, 1:200) and anti-human CD8 (Agilent, M7103, 1:200), while Doxo-treated HCT-116 cells and controls were incubated with anti-human RPL11 and anti-human MDM2 (Santa Cruz Biotechnology, sc-965, 1:100). The antibodies anti-Phospho-Histone H2A.X (Millipore, code 05-636, 1:500) and anti-Phospho ATR (GeneTex, GTX128145, 1:500) were incubated o/n at 4°C. The slice and the cells were then incubated with the appropriate fluorophore-conjugated secondary antibody. Then, they were processed for the staining with 594 conjugated-fibrillarin. The biological material was fixed again with 4% of paraformaldehyde for 5 min at room temperature, washed three times with PBS1× for 5 min, and block for 30 min with 2.5% BSA solution. Then, it was incubated o/n at 4°C with anti-human fibrillarin-594 conjugated (Santa Cruz Biotechnology, sc-166001 AF594, 1:50). The immunophenotyping on meta1 cryosection was performed with anti-CD4 (ThermoFisher, PA5-85858, 1:200) anti-mouse anti-human CD163 (BD Bioscience, clone GHI/61, cat. 562669, 1:100) antibodies. Before imaging, nuclei were counterstained with (DAPI). Cell line experiments were imaged with Axio scan, z-stack projection (0.5 μm layers) with magnification 40×. Whole specimen imaging was performed with both Axio scan and Leica TCS SP8 Stimulated Emission Depletion (STED) super-resolution microscopy and analyzed with corresponding software.

4.3.7 | β-Galactosidase enzymatic assay

Fresh surgically removed human specimens were OCT embedded and flash-frozen in liquid nitrogen. Immediately after, 10-μm-thick serial sections were cut, placed onto poly-adenylated slides, and processed for β-galactosidase staining with DBA kit (Cat#AB102534). The frozen slices were kept at room temperature for 5 min and then washed twice with PBS1× for 1 min. Then, they were fixed with a fixative solution for 10 min at room temperature, washed twice with PBS1× for 1 min, and placed in incubator at 37°C o/n with β-galactosidase staining solution provided by the kit. The day after the slides were washed three times with PBS1× and counterstained with nuclear fast red. Then, they were dehydrated with ethanol, mounted

with Eukitt, and analyzed with an Olympus BX61 virtual slide scanning. The same steps were performed also for HCT-116 treated cells and controls.

4.3.8 | Induction of cellular senescence in HCT-116 cell line and RNAseq analysis

About 2×10^5 cells were seeded into 6-well plates. After 1 day of starvation, cells were exposed to 800 nM doxorubicin (Doxo) (Merck; Cat # D1515) for 48 h. On Day 2, Doxo was replaced with fresh media and cells were followed until Day 13 with regular media changes every 4 days. Control cells were treated in parallel with DMSO 800 nM.

For RNAseq, three independent experiments were performed. RNA was extracted with RNeasy micro kit (cat. No. 74004, Qiagen) and sequenced after control quality check. The reads of the poly(A) RNAseq analysis were mapped against reference genome GRCh38 with STAR Aligner v2.7.10a (Dobin et al., 2013), and count table was generated using the function featureCounts from Rsubread package v2.12.0 (Liao et al., 2019), using exon for the reads summarization. Genes with less than 10 raw counts in 1% of the samples or with hypervariable expression found with DaMiRseq package v2.10.0 were removed (Chiesa et al., 2018). Differential gene expression analysis was performed by DESeq2 package v1.38.3. DEG genes with pvalue_adj <0.05 and log2FC >1 or log2FC ≤−1 as were included (Love et al., 2014). Pseudo-bulk conversion of SMCCs spatial transcriptional data were performed by AggregateExpression function from Seurat package.

4.3.9 | RT-qPCR assay

Cells were homogenized by cryogenic step. Total RNA was purified using Direct-zol RNA MiniPrep w/Zymo-Spin IIC Columns. cDNA synthesis was performed using Superscript Vilo cDNA Synthesis kit (Life Technologies) following manufacturer's instruction and random primers (0.5 μg/μL, Invitrogen). Real-time PCR reactions were carried out using the Fast Sybr Green PCR kit (QuantiStudio 7 Flex RrealTime PCR; Applied Biosystems). The relative expression levels were calculated by the $\Delta\Delta C_T$ method after normalization to the average of GADPH level. Primer sequences are listed above.

4.3.10 | Visium spatial gene expression data analysis

Fastq files were generated with 10× Genomics software Space Ranger v1.2.2 with spaceranger mkfastq function, quality checked with fastqc v0.11.8. The reads were aligned to the human reference transcriptome GRCh38 with spaceranger count command. The obtained count matrices were processed using R v4.0.5 and Seurat package v4.0.1. We applied the following exclusion criteria: meta1: 200 < UMIs > 12,000; 100 < features > 3500; meta2: 200 < UMIs < 8000; 100 < features < 3000; meta4: 200 < UMIs < 20,000; 100 < features < 4500; meta3:200 < UMIs < 10,000; 100 < features < 3500. The mitochondrial gene rate cutoff was >15%. Data were normalized using SCTransform function. Each dataset was first analyzed separately. The transcriptional clusters which map within liver parenchyma were removed; from the resulting four spatial transcriptomic datasets, we generated a unique integrated transcriptional map by Seurat SCTransform integration workflow, using 3000 integration features. Principal component analysis was performed with default parameters; data clustering was performed using FindNeighbors, combining the first 30 PCA dimensions with the FindClusters function Seurat R package implemented (resolution parameter = 0.4). The UMAP dimensionality reduction were generated with min.dist = 0 and n.neighbors = 9 options. The clusters were projected back into H&E images and Meta2 and Meta3 SA-β-gal stained sections to identify which transcriptional cluster overlaps with β-gala-positive areas. The individual analysis on meta1 specimen was performed accordingly to the procedure described above, with minor modifications (resolution parameter = 0.8). Cell cycle phase was extrapolated by CellCycleScoring function; spatial gene expression maps were generated by SpatialFeaturePlot function; imputed gene expression count matrix was generated by RunALRA function (SeuratWrappers package v0.3.0); EMT score was extrapolated from the EMTome database, using AddModuleScore function with default parameters. Trajectory's analysis was performed with PCA reduction, on the 3000 most highly variable genes of individual meta1 transcriptome, while the pseudotime EMT inference is generated by slingshot package v1.8.0., setting C_5 as starting cluster. eSMCC versus mSMCC Differentially Expressed Genes (DEGs) were obtained with the FindMarkers function (logfc.threshold = 0.3, min.pct = 0.2, MAST algorithm). In the volcano plot, genes were considered significant with *p*_val_adj <0.05 and avg_log2FC > 0.3 < −0.3; gene prevalence was calculated as the ratio of pct1 to pct2. GO pathway enrichment was performed on the significant DEGs, using enrichR package v3.0. GO_Biological_Process_2021 is the reference database. Regulons activity was inferred with Single-Cell Regulatory Network Inference and Clustering (SCENIC v1.2.4). The ribosome biogenesis network was reconstructed by Cytoscape v3.9.0 with STRING database. Cell states and ecotypes recovery in Visium data were performed by EcoTyper tool setting "Carcinoma" for Discovery dataset and "Epithelial.cells" for Malignant cell origin. Deconvolution of immune cell type in the spatial transcriptomic dataset was performed by scvi-tools v0.16.4 used in R with reticulate package v1.25. Finally, the eSMCC and mSMCC-specific gene signatures were obtained, selecting the top 100 DEGs based on avg_log2FC with a *p*_val_adj <0.05. Bonferroni correction was applied based on the total genes present in the dataset. Unless mentioned otherwise, all plots were generated using R package ggplot2 v3.3.5.

4.4 | Statistical analysis

Survival analysis and Kaplan–Meier curves on retrospective cohort were performed with survival v3.2-11 and survminer v0.4.9 R packages. Hazard ratio (HR) was estimated with a univariate Cox regression. Kaplan–Meier curves of TCGA patients were obtained by the online tool GEPIA2 (http://gepia2.cancer-pku.cn/); the patients were assigned to the high cohort when their signature expression was above the third quartile or to the low cohort when it was below the first one. The Wilcox test in ggpubr package v0.4.0 has been applied in all other analyses.

4.5 | Study approval

All research was conducted by both the Declarations of Helsinki and Istanbul; all research was approved by the appropriate ethics institutional review committee (IRCSS Istituto Clinico Humanitas, Prot. Nr. CE HUmaniats ex D.M. 8/2/2013 564/21). Written informed consent was received before participation.

AUTHOR CONTRIBUTIONS

O.G. and L.L. conducted the experiments and analyzed the data. L.L. performed bioinformatics analysis. G.B. performed spatial transcriptomics on human specimens. D.G. performed RNAseq experiments. C.P. provided technical support for Spatial Transcriptomics. V.M. contributed to data analysis. B.F., C.S., D.B., and F.P. contributed to immunohistochemistry experiments. G.C. contributed to human CRLM patients' statistical analysis. D.A., A. S., and T.L. contributed to histological diagnosis of CRLM patients. G.T. and M.D. contributed to human CRLM patient selection. F.F., O.G., L.L., G.C., V.M., and M.D. provided in scientific discussion. F.F. conceived the study interpreted the data and wrote the manuscript. O.G and L.L. are co–first authors since they had complementary skills, essential to achieve the final results.

ACKNOWLEDGMENTS

We thank Dr. A. Doni and Dr. F. Grizzi for their help in imaging with SP8 STED3x SMD, Dr. A. Felicetta for providing antibodies and Axio scan and Dr. Micheal Latroniko for English editing. We also thank the Genomics Facility at IRCCS Humanitas Research Hospital for the technical support. The research leading to these results has received funding from the Italian Ministry of Health, Ricerca Finalizzata (FF; GR-2016-02363222).

CONFLICT OF INTEREST STATEMENT

The authors have declared that no conflict of interest exists.

DATA AVAILABILITY STATEMENT

The raw data are available on Gene Expression Omnibus (GEO) under accession number “GSE206552”.

ORCID

Luca Lambroia https://orcid.org/0000-0002-8724-1485
Desiree Giuliano https://orcid.org/0000-0003-0576-4125
Francesca Faggioli https://orcid.org/0000-0001-8030-3674

REFERENCES

Amor, C., Feucht, J., Leibold, J., Ho, Y. J., Zhu, C., Alonso-Curbelo, D., Mansilla-Soto, J., Boyer, J. A., Li, X., Giavridis, T., Kulick, A., Houlihan, S., Peerschke, E., Friedman, S. L., Ponomarev, V., Piersigilli, A., Sadelain, M., & Lowe, S. W. (2020). Senolytic CAR T cells reverse senescence-associated pathologies. *Nature*, *583*(7814), 127–132. https://doi.org/10.1038/s41586-020-2403-9

Baba, A. B., Rah, B., Bhat, G. R., Mushtaq, I., Parveen, S., Hassan, R., Hameed Zargar, M., & Afroze, D. (2022). Transforming growth factor-Beta (TGF-β) signaling in cancer-a betrayal within. *Frontiers in Pharmacology*, *13*, 791272. https://doi.org/10.3389/fphar.2022.791272

Basisty, N., Kale, A., Jeon, O. H., Kuehnemann, C., Payne, T., Rao, C., Holtz, A., Shah, S., Sharma, V., Ferrucci, L., Campisi, J., & Schilling, B. (2020). A proteomic atlas of senescence-associated secretomes for aging biomarker development. *PLoS Biology*, *18*(1), e3000599. https://doi.org/10.1371/journal.pbio.3000599

Bennecke, M., Kriegl, L., Bajbouj, M., Retzlaff, K., Robine, S., Jung, A., Arkan, M. C., Kirchner, T., & Greten, F. R. (2010). Ink4a/Arf and oncogene-induced senescence prevent tumor progression during alternative colorectal tumorigenesis. *Cancer Cell*, *18*(2), 135–146. https://doi.org/10.1016/j.ccr.2010.06.013

Bird, T. G., Müller, M., Boulter, L., Vincent, D. F., Ridgway, R. A., Lopez-Guadamillas, E., Lu, W. Y., Jamieson, T., Govaere, O., Campbell, A. D., Ferreira-Gonzalez, S., Cole, A. M., Hay, T., Simpson, K. J., Clark, W., Hedley, A., Clarke, M., Gentaz, P., Nixon, C., … Forbes, S. J. (2018). TGFβ inhibition restores a regenerative response in acute liver injury by suppressing paracrine senescence. *Science Translational Medicine*, *10*, eaan1230.

Birkbak, N. J., & McGranahan, N. (2020). Cancer genome evolutionary trajectories in metastasis. *Cancer Cell*, *37*, 8–19. https://doi.org/10.1016/j.ccell.2019.12.004

Boulon, S., Westman, B. J., Hutten, S., Boisvert, F. M., & Lamond, A. I. (2010). The nucleolus under stress. *Molecular Cell*, *40*, 216–227. https://doi.org/10.1016/j.molcel.2010.09.024

Braig, M., & Schmitt, C. A. (2006). Oncogene-induced senescence: Putting the brakes on tumor development. *Cancer Research*, *66*, 2881–2884. https://doi.org/10.1158/0008-5472.CAN-05-4006

Burri, N., Shaw, P., Bouzourene, H., Sordat, I., Sordat, B., Gillet, M., Schorderet, D., Bosman, F. T., & Chaubert, P. (2001). *Methylation silencing and mutations of the p14 ARF and p16 INK4a genes in colon cancer.*

Bursać, S., Brdovčak, M. C., Pfannkuchen, M., Orsolić, I., Golomb, L., Zhu, Y., Katz, C., Daftuar, L., Grabušić, K., Vukelić, I., Filić, V., Oren, M., Prives, C., & Volarevic, S. (2012). Mutual protection of ribosomal proteins L5 and L11 from degradation is essential for p53 activation upon ribosomal biogenesis stress. *Proceedings of the National Academy of Sciences of the United States of America*, *109*(50), 20467–20472. https://doi.org/10.1073/pnas.1218535109

Cagnoni, A. J., Giribaldi, M. L., Blidner, A. G., Cutine, A. M., Gatto, S. G., Morales, R. M., Salatino, M., Abba, M. C., Croci, D. O., Mariño, K. V., & Rabinovich, G. A. (2021). Galectin-1 fosters an immunosuppressive microenvironment in colorectal cancer by reprogramming $CD8^+$ regulatory T cells. *Proceedings of the National Academy of Sciences*, *118*(21), e2102950118. https://doi.org/10.1073/pnas.2102950118

Campisi, J., & D'Adda Di Fagagna, F. (2007). Cellular senescence: When bad things happen to good cells. *Nature Reviews Molecular Cell Biology*, *8*, 729–740. https://doi.org/10.1038/nrm2233

Celià-Terrassa, T., & Kang, Y. (2018). Metastatic niche functions and therapeutic opportunities. *Nature Cell Biology*, *20*, 868–877. https://doi.org/10.1038/s41556-018-0145-9

Che, L. H., Liu, J. W., Huo, J. P., Luo, R., Xu, R. M., He, C., Li, Y. Q., Zhou, A. J., Huang, P., Chen, Y. Y., Ni, W., Zhou, Y. X., Liu, Y. Y., Li, H. Y., Zhou, R., Mo, H., & Li, J. M. (2021). A single-cell atlas of liver metastases of colorectal cancer reveals reprogramming of the tumor microenvironment in response to preoperative chemotherapy. *Cell Discovery*, *7*(1), 1–21. https://doi.org/10.1038/s41421-021-00312-y

Chen, C., Li, L., Zhou, H. J., & Min, W. (2017). The role of NOX4 and TRX2 in angiogenesis and their potential cross-talk. *Antioxidants*, *6*, 42. https://doi.org/10.3390/antiox6020042

Chen, H. A., Ho, Y. J., Mezzadra, R., Adrover, J. M., Smolkin, R., Zhu, C., Woess, K., Bernstein, N., Schmitt, G., Fong, L., Luan, W., Wuest, A., Tian, S., Li, X., Broderick, C., Hendrickson, R. C., Egeblad, M., Chen, Z., Alonso-Curbelo, D., & Lowe, S. W. (2022). Senescence rewires microenvironment sensing to facilitate anti-tumor immunity. *Cancer Discovery*, *13*, 432–453. https://doi.org/10.1158/2159-8290.CD-22-0528

Chiavarina, B., Costanza, B., Ronca, R., Blomme, A., Rezzola, S., Chiodelli, P., Giguelay, A., Belthier, G., Doumont, G., Van Simaeys, G., Lacroix, S., Yokobori, T., Erkhem-Ochir, B., Balaguer, P., Cavailles, V., Fabbrizio, E., Di Valentin, E., Gofflot, S., Detry, O., … Turtoi, A. (2021). Metastatic colorectal cancer cells maintain the TGFβ program and use TGFBI to fuel angiogenesis. *Theranostics*, *11*(4), 1626–1640. https://doi.org/10.7150/thno.51507

Chiesa, M., Colombo, G. I., & Piacentini, L. (2018). DaMiRseq – An R/bioconductor package for data mining of RNA-seq data: Normalization, feature selection and classification. *Bioinformatics*, *34*(8), 1416–1418. https://doi.org/10.1093/bioinformatics/btx795

Choi, Y. W., Kim, Y. H., Oh, S. Y., Suh, K. W., Kim, Y. S., Lee, G. Y., Yoon, J. E., Park, S. S., Lee, Y. K., Park, Y. J., Kim, H. S., Park, S. H., Kim, J. H., & Park, T. J. (2021). Senescent tumor cells build a cytokine shield in colorectal cancer. *Advanced Science*, *8*(4), 2002497. https://doi.org/10.1002/advs.202002497

Debacq-Chainiaux, F., Erusalimsky, J. D., Campisi, J., & Toussaint, O. (2009). Protocols to detect senescence-associated beta-galactosidase (SA-βgal) activity, a biomarker of senescent cells in culture and in vivo. *Nature Protocols*, *4*(12), 1798–1806. https://doi.org/10.1038/nprot.2009.191

Desai, L. P., Zhou, Y., Estrada, A. V., Ding, Q., Cheng, G., Collawn, J. F., & Thannickal, V. J. (2014). Negative regulation of NADPH oxidase 4 by hydrogen peroxide-inducible clone 5 (hic-5) protein. *Journal of Biological Chemistry*, *289*(26), 18270–18278. https://doi.org/10.1074/jbc.M114.562249

Destefanis, F., Manara, V., & Bellosta, P. (2020). Myc as a regulator of ribosome biogenesis and cell competition: A link to cancer. *International Journal of Molecular Sciences*, *21*, 1–19. https://doi.org/10.3390/ijms21114037

Dobin, A., Davis, C. A., Schlesinger, F., Drenkow, J., Zaleski, C., Jha, S., Batut, P., Chaisson, M., & Gingeras, T. R. (2013). STAR: Ultrafast universal RNA-seq aligner. *Bioinformatics*, *29*(1), 15–21. https://doi.org/10.1093/bioinformatics/bts635

Faggioli, F., Velarde, M. C., & Wiley, C. D. (2023). Cellular senescence, a novel area of investigation for metastatic diseases. *Cell*, *12*(6), 860. https://doi.org/10.3390/cells12060860

Giessler, K. M., Kleinheinz, K., Huebschmann, D., Balasubramanian, G. P., Dubash, T. D., Dieter, S. M., Siegl, C., Herbst, F., Weber, S., Hoffmann, C. M., Fronza, R., Buchhalter, I., Paramasivam, N., Eils, R., Schmidt, M., von Kalle, C., Schneider, M., Ulrich, A., Scholl, C., Fröhling, S., … Glimm, H. (2017). Genetic subclone architecture of tumor clone-initiating cells in colorectal cancer. *The Journal of experimental medicine*, *214*(7), 2073–2088. https://doi.org/10.1084/jem.20162017

Gorgoulis, V., Adams, P. D., Alimonti, A., Bennett, D. C., Bischof, O., Bishop, C., Campisi, J., Collado, M., Evangelou, K., Ferbeyre, G., Gil, J., Hara, E., Krizhanovsky, V., Jurk, D., Maier, A. B., Narita, M., Niedernhofer, L., Passos, J. F., Robbins, P. D., … Demaria, M. (2019). Cellular senescence: Defining a path forward. *Cell*, *179*, 813–827. https://doi.org/10.1016/j.cell.2019.10.005

Hannon, G. J., & Beach, D. (1994). pI5INK4B is a potentia| effector of TGF-β-induced cell cycle arrest. *Nature*, *371*(6494), 257–261. https://doi.org/10.1038/371257a0

Haugstetter, A. M., Loddenkemper, C., Lenze, D., Gröne, J., Standfuss, C., Petersen, I., Dörken, B., & Schmitt, C. A. (2010). Cellular senescence predicts treatment outcome in metastasised colorectal cancer. *British Journal of Cancer*, *103*(4), 505–509. https://doi.org/10.1038/sj.bjc.6605784

Havel, J. J., Li, Z., Cheng, D., Peng, J., & Fu, H. (2015). Nuclear PRAS40 couples the Akt/mTORC1 signaling axis to the RPL11-HDM2-p53 nucleolar stress response pathway. *Oncogene*, *34*(12), 1487–1498. https://doi.org/10.1038/onc.2014.91

Hayflick, L., & Moorhead, P. S. (1961). The serial cultivation of human diploid cell strains. *Experimental Cell Research*, *25*(3), 585–621. https://doi.org/10.1016/0014-4827(61)90192-6

Hernandez-Segura, A., de Jong, T. V., Melov, S., Guryev, V., Campisi, J., & Demaria, M. (2017). Unmasking transcriptional heterogeneity in senescent cells. *Current Biology*, *27*(17), 2652–2660.e4. https://doi.org/10.1016/j.cub.2017.07.033

Hu, Z., Ding, J., Ma, Z., Sun, R., Seoane, J. A., Scott Shaffer, J., Suarez, C. J., Berghoff, A. S., Cremolini, C., Falcone, A., Loupakis, F., Birner, P., Preusser, M., Lenz, H. J., & Curtis, C. (2019). Quantitative evidence for early metastatic seeding in colorectal cancer. *Nature Genetics*, *51*(7), 1113–1122. https://doi.org/10.1038/s41588-019-0423-x

Jones, S., Chen, W. D., Parmigiani, G., Diehl, F., Beerenwinkel, N., Antal, T., Traulsen, A., Nowak, M. A., Siegel, C., Velculescu, V. E., Kinzler, K. W., Vogelstein, B., Willis, J., & Markowitz, S. D. (2008). Comparative lesion sequencing provides insights into tumor evolution. *Proceedings of the National Academy of Sciences of the United States of America*, *105*(11), 4283–4288. https://doi.org/10.1073/pnas.0712345105

Kalluri, R., & Weinberg, R. A. (2009). The basics of epithelial-mesenchymal transition. *Journal of Clinical Investigation*, *119*, 1420–1428. https://doi.org/10.1172/JCI39104

Kang, T. W., Yevsa, T., Woller, N., Hoenicke, L., Wuestefeld, T., Dauch, D., Hohmeyer, A., Gereke, M., Rudalska, R., Potapova, A., Iken, M., Vucur, M., Weiss, S., Heikenwalder, M., Khan, S., Gil, J., Bruder, D., Manns, M., Schirmacher, P., … Zender, L. (2011). Senescence surveillance of pre-malignant hepatocytes limits liver cancer development. *Nature*, *479*(7374), 547–551. https://doi.org/10.1038/nature10599

Kim, Y. H., Choi, Y. W., Lee, J., Soh, E. Y., Kim, J. H., & Park, T. J. (2017). Senescent tumor cells lead the collective invasion in thyroid cancer. *Nature Communications*, *10*(8), 15208. https://doi.org/10.1038/ncomms15208

Kumari, R., & Jat, P. (2021). Mechanisms of cellular senescence: Cell cycle arrest and senescence associated secretory phenotype. *Frontiers in Cell and Developmental Biology*, *9*, 645593. https://doi.org/10.3389/fcell.2021.645593

Li, D., Shu, X., Zhu, P., & Pei, D. (2021). Chromatin accessibility dynamics during cell fate reprogramming. *EMBO Reports*, *22*(2), e51644. https://doi.org/10.15252/embr.202051644

Liao, Y., Smyth, G. K., & Shi, W. (2019). The R package Rsubread is easier, faster, cheaper and better for alignment and quantification of RNA sequencing reads. *Nucleic Acids Research*, *47*(8), e47. https://doi.org/10.1093/nar/gkz114

Liu, J. F., Wu, L., Yang, L. L., Deng, W. W., Mao, L., Wu, H., Zhang, W. F., & Sun, Z. J. (2018). Blockade of TIM3 relieves immunosuppression

through reducing regulatory T cells in head and neck cancer. *Journal of Experimental and Clinical Cancer Research*, *37*(1), 44. https://doi.org/10.1186/s13046-018-0713-7

Lloyd, R. V., Erickson, L. A., Jin, L., Kulig, E., Qian, X., Cheville, J. C., & Scheithauer, B. W. (1999). p27kip1: A multifunctional cyclin-dependent kinase inhibitor with prognostic significance in human cancers. *The American Journal of Pathology*, *154*(2), 313–323. https://doi.org/10.1016/S0002-9440(10)65277-7

Lohrum, M. A. E., Ludwig, R. L., Kubbutat, M. H. G., Hanlon, M., & Vousden, K. H. (2000). *Regulation of HDM2 activity by the ribosomal protein L11*.

Love, M. I., Huber, W., & Anders, S. (2014). Moderated estimation of fold change and dispersion for RNA-seq data with DESeq2. *Genome Biology*, *15*(12), 550. https://doi.org/10.1186/s13059-014-0550-8

Luca, B. A., Steen, C. B., Matusiak, M., Azizi, A., Varma, S., Zhu, C., Przybyl, J., Espín-Pérez, A., Diehn, M., Alizadeh, A. A., van de Rijn, M., Gentles, A. J., & Newman, A. M. (2021). Atlas of clinically distinct cell states and ecosystems across human solid tumors. *Cell*, *184*(21), 5482–5496.e28. https://doi.org/10.1016/j.cell.2021.09.014

Luzzi, K. J., MacDonald, I. C., Schmidt, E. E., Kerkvliet, N., Morris, V. L., Chambers, A. F., & Groom, A. C. (1998). Multistep nature of metastatic inefficiency. *The American Journal of Pathology*, *153*(3), 865–873. https://doi.org/10.1016/S0002-9440(10)65628-3

Mahner, S., Baasch, C., Schwarz, J., Hein, S., Wölber, L., Jänicke, F., & Milde-Langosch, K. (2008). C-Fos expression is a molecular predictor of progression and survival in epithelial ovarian carcinoma. *British Journal of Cancer*, *99*(8), 1269–1275. https://doi.org/10.1038/sj.bjc.6604650

Maréchal, A., & Zou, L. (2013). DNA damage sensing by the ATM and ATR kinases. *Cold Spring Harbor Perspectives in Biology*, *5*(9), a012716. https://doi.org/10.1101/cshperspect.a012716

Marin, I., Boix, O., Garcia-Garijo, A., Sirois, I., Caballe, A., Zarzuela, E., Ruano, I., Attolini, C. S., Prats, N., López-Domínguez, J. A., Kovatcheva, M., Garralda, E., Muñoz, J., Caron, E., Abad, M., Gros, A., Pietrocola, F., & Serrano, M. (2023). Cellular senescence is immunogenic and promotes antitumor immunity. *Cancer Discovery*, *13*(2), 410–431. https://doi.org/10.1158/2159-8290.CD-22-0523

Massagué, J. (2008). TGFβ in cancer. *Cell*, *134*, 215–230. https://doi.org/10.1016/j.cell.2008.07.001

Michaloglou, C., Vredeveld, L. C. W., Mooi, W. J., & Peeper, D. S. (2008). BRAFE600 in benign and malignant human tumours. *Oncogene*, *27*, 877–895. https://doi.org/10.1038/sj.onc.1210704

Milanovic, M., Fan, D. N. Y., Belenki, D., Däbritz, J. H. M., Zhao, Z., Yu, Y., Dörr, J. R., Dimitrova, L., Lenze, D., Monteiro Barbosa, I. A., Mendoza-Parra, M. A., Kanashova, T., Metzner, M., Pardon, K., Reimann, M., Trumpp, A., Dörken, B., Zuber, J., Gronemeyer, H., … Schmitt, C. A. (2018). Senescence-associated reprogramming promotes cancer stemness. *Nature*, *553*(7686), 96–100. https://doi.org/10.1038/nature25167

Morgado-Palacin, L., Llanos, S., Urbano-Cuadrado, M., Blanco-Aparicio, C., Megias, D., Pastor, J., & Serrano, M. (2014). Non-genotoxic activation of p53 through the RPL11-dependent ribosomal stress pathway. *Carcinogenesis*, *35*(12), 2820–2830. https://doi.org/10.1093/carcin/bgu220

Muñoz-Espín, D., & Serrano, M. (2014). Cellular senescence: From physiology to pathology. *Nature Reviews Molecular Cell Biology*, *15*, 482–496. https://doi.org/10.1038/nrm3823

Naylor, R. M., Baker, D. J., & van Deursen, J. M. (2013). Senescent cells: A novel therapeutic target for aging and age-related diseases. *Clinical Pharmacology and Therapeutics*, *93*(1), 105–116. https://doi.org/10.1038/clpt.2012.193

Ou, H. L., Hoffmann, R., González-López, C., Doherty, G. J., Korkola, J. E., & Muñoz-Espín, D. (2021). Cellular senescence in cancer: From mechanisms to detection. *Molecular Oncology*, *15*(10), 2634–2671.

Ovadya, Y., & Krizhanovsky, V. (2018). Strategies targeting cellular senescence. *Journal of Clinical Investigation*, *128*, 1247–1254. https://doi.org/10.1172/JCI95149

Pastushenko, I., Brisebarre, A., Sifrim, A., Fioramonti, M., Revenco, T., Boumahdi, S., Van Keymeulen, A., Brown, D., Moers, V., Lemaire, S., De Clercq, S., Minguijón, E., Balsat, C., Sokolow, Y., Dubois, C., De Cock, F., Scozzaro, S., Sopena, F., Lanas, A., … Blanpain, C. (2018). Identification of the tumour transition states occurring during EMT. *Nature*, *556*(7702), 463–468. https://doi.org/10.1038/s41586-018-0040-3

Patry, M., Teinturier, R., Goehrig, D., Zetu, C., Ripoche, D., Kim, I. S., Bertolino, P., & Hennino, A. (2015). βig-h3 represses T-cell activation in type 1 diabetes. *Diabetes*, *64*(12), 4212–4219. https://doi.org/10.2337/db15-0638

Petrova, N. v., Velichko, A. K., Razin, S. V., & Kantidze, O. L. (2016). Small molecule compounds that induce cellular senescence. *Aging Cell*, *15*, 999–1017. https://doi.org/10.1111/acel.12518

Podhorecka, M., Skladanowski, A., & Bozko, P. (2010). H2AX phosphorylation: Its role in DNA damage response and cancer therapy. *Journal of Nucleic Acids*, *2010*, 1–9. https://doi.org/10.4061/2010/920161

Roberson, R. S., Kussick, S. J., Vallieres, E., Chen, S.-Y. J., & Wu, D. Y. (2005). Escape from therapy-induced accelerated cellular senescence in p53-null lung cancer cells and in human lung cancers. *Cancer Research*, *65*, 2795–2803.

Russo, A., & Russo, G. (2017). Ribosomal proteins control or bypass p53 during nucleolar stress. *International Journal of Molecular Sciences*, *18*, 140. https://doi.org/10.3390/ijms18010140

Saleh, T., Tyutyunyk-Massey, L., Patel, N. H., Cudjoe, E. K., Alotaibi, M., & Gewirtz, D. A. (2020). Studies of non-protective autophagy provide evidence that recovery from therapy-induced senescence is independent of early autophagy. *International Journal of Molecular Sciences*, *21*(4), 1427. https://doi.org/10.3390/ijms21041427

Salminen, A., Kauppinen, A., & Kaarniranta, K. (2012). Emerging role of NF-κB signaling in the induction of senescence-associated secretory phenotype (SASP). *Cellular Signalling*, *24*, 835–845. https://doi.org/10.1016/j.cellsig.2011.12.006

Senturk, S., Gursoy-Yuzugullu, O., Cingoz, B., Akcali, K. C., & Ozturk, M. (2010). Transforming growth factor-beta induces senescence in hepatocellular carcinoma cells and inhibits tumor growth. *Hepatology*, *52*(3), 966–974. https://doi.org/10.1002/hep.23769

Seoane, J., & Gomis, R. R. (2017). TGF-β family signaling in tumor suppression and cancer progression. *Cold Spring Harbor Perspectives in Biology*, *9*, a022277. https://doi.org/10.1101/cshperspect.a022277

Sieben, C. J., Sturmlechner, I., van de Sluis, B., & van Deursen, J. M. (2018). Two-step senescence-focused cancer therapies. *Trends in Cell Biology*, *28*, 723–737. https://doi.org/10.1016/j.tcb.2018.04.006

Smit, M. A., & Peeper, D. S. (2010). *Epithelial-mesenchymal transition and senescence: Two cancer-related processes are crossing paths*. (Vol. 2). www.impactaging.com

Sonzogni, S. V., Ogara, M. F., Belluscio, L. M., Castillo, D. S., Scassa, M. E., & Cánepa, E. T. (2014). P19INK4d is involved in the cellular senescence mechanism contributing to heterochromatin formation. *Biochimica et Biophysica Acta – General Subjects*, *1840*(7), 2171–2183. https://doi.org/10.1016/j.bbagen.2014.03.015

Steeg, P. S. (2006). Tumor metastasis: Mechanistic insights and clinical challenges. *Nature Medicine*, *12*, 895–904. https://doi.org/10.1038/nm1469

Tauriello, D. V. F., Sancho, E., & Batlle, E. (2022). Overcoming TGFβ-mediated immune evasion in cancer. *Nature Reviews Cancer*, *22*, 25–44. https://doi.org/10.1038/s41568-021-00413-6

Tirosh, I., Izar, B., Prakadan, S. M., Wadsworth, M. H., 2nd, Treacy, D., Trombetta, J. J., Rotem, A., Rodman, C., Lian, C., Murphy, G., Fallahi-Sichani, M., Dutton-Regester, K., Lin, J. R., Cohen, O., Shah, P., Lu, D., Genshaft, A. S., Hughes, T. K., Ziegler, C. G., … Garraway, L. A. (2016). Dissecting the multicellular ecosystem of metastatic melanoma by single-cell RNA-seq. *Science*, *352*(6282), 189–196. https://doi.org/10.1126/science.aad0501

vander Ark, A., Cao, J., & Li, X. (2018). TGF-β receptors: In and beyond TGF-β signaling. *Cellular Signalling*, *52*, 112–120. https://doi.org/10.1016/j.cellsig.2018.09.002

Vasaikar, S. V., Deshmukh, A. P., den Hollander, P., Addanki, S., Kuburich, N. A., Kudaravalli, S., Joseph, R., Chang, J. T., Soundararajan, R., & Mani, S. A. (2021). EMTome: A resource for pan-cancer analysis of epithelial-mesenchymal transition genes and signatures. *British Journal of Cancer*, *124*(1), 259–269. https://doi.org/10.1038/s41416-020-01178-9

Waldman, A. D., Fritz, J. M., & Lenardo, M. J. (2020). A guide to cancer immunotherapy: From T cell basic science to clinical practice. *Nature Reviews Immunology*, *20*, 651–668. https://doi.org/10.1038/s41577-020-0306-5

Was, H., Czarnecka, J., Kominek, A., Barszcz, K., Bernas, T., Piwocka, K., & Kaminska, B. (2018). Some chemotherapeutics-treated colon cancer cells display a specific phenotype being a combination of stem-like and senescent cell features. *Cancer Biology and Therapy*, *19*(1), 63–75. https://doi.org/10.1080/15384047.2017.1385675

Winkler, J., Abisoye-Ogunniyan, A., Metcalf, K. J., & Werb, Z. (2020). Concepts of extracellular matrix remodelling in tumour progression and metastasis. *Nature Communications*, *11*, 5120. https://doi.org/10.1038/s41467-020-18794-x

Wolfgang Doppler, P. J.-D. (2019). Regulation of mitochondrial ROS production by HIC-5: A common feature of oncogene-induced senescence and tumor invasiveness? *FEBS*, *286*, 456–458.

Xue, W., Zender, L., Miething, C., Dickins, R. A., Hernando, E., Krizhanovsky, V., Cordon-Cardo, C., & Lowe, S. W. (2007). Senescence and tumour clearance is triggered by p53 restoration in murine liver carcinomas. *Nature*, *445*(7128), 656–660. https://doi.org/10.1038/nature05529

Yang, K., Yang, J., & Yi, J. (2018). Nucleolar stress: Hallmarks, sensing mechanism and diseases. *Cell Stress*, *2*, 125–140. https://doi.org/10.15698/cst2018.06.139

Yang, L., Fang, J., & Chen, J. (2017). Tumor cell senescence response produces aggressive variants. *Cell Death Discovery*, *3*(1), 17049. https://doi.org/10.1038/cddiscovery.2017.49

Zhou, H., Liu, Z., Wang, Y., Wen, X., Amador, E. H., Yuan, L., Ran, X., Xiong, L., Ran, Y., Chen, W., & Wen, Y. (2022). Colorectal liver metastasis: Molecular mechanism and interventional therapy. *Signal Transduction and Targeted Therapy*, *7*, 70. https://doi.org/10.1038/s41392-022-00922-2

SUPPORTING INFORMATION

Additional supporting information can be found online in the Supporting Information section at the end of this article.

How to cite this article: Garbarino, O., Lambroia, L., Basso, G., Marrella, V., Franceschini, B., Soldani, C., Pasqualini, F., Giuliano, D., Costa, G., Peano, C., Barbarossa, D., Annarita, D., Salvati, A., Terracciano, L., Torzilli, G., Donadon, M., & Faggioli, F. (2023). Spatial resolution of cellular senescence dynamics in human colorectal liver metastasis. *Aging Cell*, *22*, e13853. https://doi.org/10.1111/acel.13853